HAL
open science

First Principles Modelling of Dye Anchoring on (001) g-Monoclinic WO 3 Surfaces: The Role of Oxygen Vacancies

Azza Ben Jannet, Moncef Said, Michael Badawi, Mariachiara Pastore

To cite this version:

Azza Ben Jannet, Moncef Said, Michael Badawi, Mariachiara Pastore. First Principles Modelling of Dye Anchoring on (001) g-Monoclinic WO 3 Surfaces: The Role of Oxygen Vacancies. Journal of Physical Chemistry C, 2022, 126 (12), pp.5424-5434. 10.1021/acs.jpcc.1c10397 . hal-03871114

HAL Id: hal-03871114

https://hal.science/hal-03871114v1

Submitted on 25 Nov 2022

HAL is a multi-disciplinary open access archive for the deposit and dissemination of scientific research documents, whether they are published or not. The documents may come from teaching and research institutions in France or abroad, or from public or private research centers.

L'archive ouverte pluridisciplinaire **HAL**, est destinée au dépôt et à la diffusion de documents scientifiques de niveau recherche, publiés ou non, émanant des établissements d'enseignement et de recherche français ou étrangers, des laboratoires publics ou privés.

Distributed under a Creative Commons Attribution 4.0 International License

First Principles Modelling of Dye Anchoring on (001) γ-Monoclinic WO_3 Surfaces: The Role of Oxygen Vacancies

Azza Ben Jannet,[a,b] Moncef Said,[a] Michael Badawi,[b] Mariachiara Pastore[b,*]

[a] Université de Monastir, Faculté des Sciences de Monastir, Laboratoire de la Matière Condensée et des Nanosciences (LMCN), LR11ES40, Avenue de l'Environnement, 5000, Monastir, Tunisie.

[b] Laboratoire de Physique et Chimie Théoriques (LPCT), Université de Lorraine & CNRS, UMR7019, 54500 Vandoeuvre-Les-Nancy, France.

*corresponding author: mariachiara.pastore@univ-lorraine.fr

Keywords: γ-Monoclinic WO_3; oxygen vacancies; dye adsorption; photocatalysis; DFT

Abstract

Here we focus on the dye's anchoring mechanism onto the (001) monoclinic WO_3 surface. We present first-principles simulations, based on density functional theory (DFT), to get atomistic insights of the adsorption of three different anchoring groups (Benzoic acid (BA), Catechol (Cat), Phenylphosphonic acid (PA)) onto the clean and oxygen-defective (001) WO_3 surfaces, considering implicit solvation effects and dispersion corrections. The results show that both BA and PA preferably adsorb in a molecular monodentate binding mode on clean surface, while the presence of oxygen vacancies on the surface makes the dissociative bidentate bridging the preferred binding mode. In the case of Cat molecule, two configurations were found to be close in energy in solution on clean surfaces, whereas the mono-deprotonated monodentate mode is the most stable one on defective surfaces. The presence of oxygen vacancies on the surface increases, in absolute value, the adsorption energies of the anchoring groups, without affecting their relative stability. The present results, providing for the first time atomic-scale details on the dye anchoring mechanism on monoclinic WO_3 substates and indicating un unfavorable W-W distance pattern on the surface (001) surface for anchoring traditional carboxylic, phosphonic and catechol anchoring groups, may suggest novel design rules for the optimization and the selection of alternative anchoring functionalities for WO_3-based DSSCs and hybrid photocatalysts.

Introduction

Among renewable energies the sun is by far the most abundant source, with irradiation of the earth's surface at a rate of 1.2×10^5 TW, largely exceeding the current worldwide power demand. By the way, to be exploitable, solar energy has to be converted in heat, electricity or "stored" in chemical bonds (fuels).[1–5] Among the different pathways available to produce solar fuels[5], artificial photosynthesis, mimicking natural photosynthesis, uses sun light to split water into H_2 and O_2.[6] In this context, photoelectrocatalytic cell (PECs) require assembly of three key units to collect solar light and perform the water splitting reaction: a light absorber, a water reduction and a water oxidation catalysts.[7–9] Hybrid photoanodes and photocathodes, obtained by functionalizing n- and p-type semiconductor nanoparticles with molecular dye sensitizers and catalysts are, indeed, an appealing approach to photoelectrochemical water splitting,[9–11] which allows to separate and optimize the three main steps required to convert sunlight into chemical bond energies, namely, i) light absorption (dye), ii) charge carriers separation/transportation (semiconductors) and iii) chemical reactions (molecular catalysts). Moreover, an alternative approach, which has the advantage of reducing the complexity of the molecules/oxide interface and minimizing the shortcomings related to the optimization of dye/catalyst ratio on the surface and to the poor stability of the molecular components, is to use the semiconductor for light harvesting and the molecular component as a catalyst for water splitting.[12–15] On the semiconductor side, different materials have been reported[16,17] for both water reduction[18–22] and oxydation.[23–30] Among the different semiconductors, tungsten trioxide, WO_3 has received particular attention in photocatalytic applications[31–36 25,26,37–45] because of its good charge carrier transport properties,[46–49] high stability against photo-corrosion under acidic condition,[50,51] and fast water oxidation kinetics.[52]

The interface (linking) between the molecular components and the semiconductor is of pivotal importance in determining the charge transfer and separation properties as well as the device stability.[53–56] Dyes and catalysts can interact with the metal oxide surface through different mechanisms, including covalent attachment, electrostatic interaction, hydrogen bonding, hydrophobic interaction, van der Waals forces, or physical entrapment.[57] Covalent adsorption by chemical bonding is by far the most employed functionalization strategy, allowing for a better control of the molecules packing and enhanced electronic coupling and charge transfer rates. Therefore, chemical grafting represents one of the most important points to address for efficient assembling of hybrid PECs and dye-sensitized solar cells. Historically, carboxylic and cyanoacrylic acids are the most employed anchoring groups for both *n*- and p-type photoelectrodes,[58–63] although they show poor stability in water environments. On the other hand, phosphonic acid provides excellent anchoring stability, with an adsorption strength estimated to be approximately 80 times higher than that of the carboxylic acid, and negligible desorption in the presence of water.[63,64] Many alternative anchoring groups have been proposed and been tested,[57] such as hydroxyl groups[60]. Contrarily to the deep knowledge and characterization that has been achieved on the grafting mechanism of dye and catalysts on TiO_2 nanoparticles, only a few experimental studies, addressing adsorption on WO_3 substrates, are available in the literature.[65–70] Bishop et al.[69] studied the binding of citric acid to different metal oxide nanoparticles (ZnO, TiO_2, Fe_2O_3, and WO_3), finding a weak adsorption onto the WO_3 surface, that was attributed to its extremely low isoelectric point. WO_3 functionalization with polydopamine (PDA) has been also reported in the context photocatalysis and immunosensor devices,[65,70] indicating the formation of a stable interface between PDA and WO_3 via catechol functionalities. Also, the binding constants of the $[Ru(bpy)_3]^{2+}$ dye anchored by either a phosphonate or an hydroxamate group to TiO_2 and

WO_3 surfaces was reported in Ref.[68], revealing, again, a stronger dye binding and a higher surface coverage on TiO_2 than on WO_3. The lower isoelectric point of WO_3 and the differences in the acidity of Lewis sites between the two metal ions (Ti^{4+} serves as stronger Lewis's acid site compared to that of W^{6+}) were individuated as the main reasons of the different binding constants. Then, concerning defective WO_3 surfaces, the adsorption mode of aliphatic alcohols on oxidized and reduced WO_3 (001) surfaces was experimentally reported in Refs.[71,72] Based on UPS measurements, methanol was found to molecularly adsorb on the oxidized surface and dissociatively adsorb on the reduced surface, and the difference was attributed to the heterogeneity of the oxidized WO_3 (001) surface, showing unfavorable distances between the acid/base pairs sites required to realize a dissociative grafting. Recently, Zhao et al.[73] reported the impact of the physical and chemical defects in γ-WO_3 (001) surface on the photocatalytic water splitting activity, showing that an appropriate amount of oxygen vacancies[73,74] results in an increased adsorption of OH groups on the metal oxide surface and in a boosted catalytic activity.

This brief overview, clearly, reveals a lack of fundamental understanding in the interaction mechanism of traditional anchoring groups with clean and defective WO_3 substrates, that would definitely require a more systematic investigation. To this respect, quantum mechanical calculations have been widely applied to study the interface phenomena in molecule-functionalized semiconductors,[60–62,75–77] and are a valuable tool for provide atomistic insights of dyes' anchoring group interactions with metal oxide surface. But, again, while a large number of theoretical studies on the dye adsorption modes on the TiO_2 surface have been reported (see for instance Refs[57,78], and references therein), to the best of our knowledge, the theoretical characterization of the adsorption mechanism of common anchoring groups on WO_3 surfaces has not be afforded yet.

To address this specific issue related to the dye/WO_3 interface, here, we consider three commonly employed anchoring groups, namely Benzoic acid (BA), Catechol (Cat) and Phenylphosphonic acid (PA) (Figure 1) and we model their adsorption onto the clean and oxygen-defective (001) surfaces of monoclinic WO_3, taking into account implicit solvation effects and dispersion corrections. Although here we are using simplified models (basically restricted to the anchoring functionality) to get information on the adsorption mechanism of realistic dye sensitizers bearing these anchoring groups, it is worthwhile to stress that this is a common practice when investigating the dye/semiconductor interactions and that the conclusions drown on small anchoring prototypes, on overall, still hold for the larger dye molecules, being the adsorption mainly driven by local interaction between the surface atoms and the anchoring unit.[56,79] Several experimental and theoretical works have, indeed, shown similar adsorption behavior for different dyes/organic molecules, bearing similar functional groups, depending on the metal oxide surface.[80–88] Evanko et al.[80] showed that the adsorption of organic acids, comprising double ring compounds, resembled the adsorption of smaller molecular weight organic acids with similar functionalities. Organic dyes often contain only one anchoring group, and their grafting properties are generally the same of those of their anchoring groups: for example, adsorption of perylene-carboxylic and perylene-phosphonic acids[87,89] is similar to that of formic[75,90] and phosphonic[76,87] acids, respectively. Similarly, O'Rourke et al.[88] found a very little difference in the adsorption geometries between a simple model of the anchoring groups and the complete dye, with the largest change amounting to 2%. Thus, we can safely affirm that the present results obtained by using prototype molecules are still representative of the adsorption mechanism of realistic dye-sensitizers or molecular catalysts.

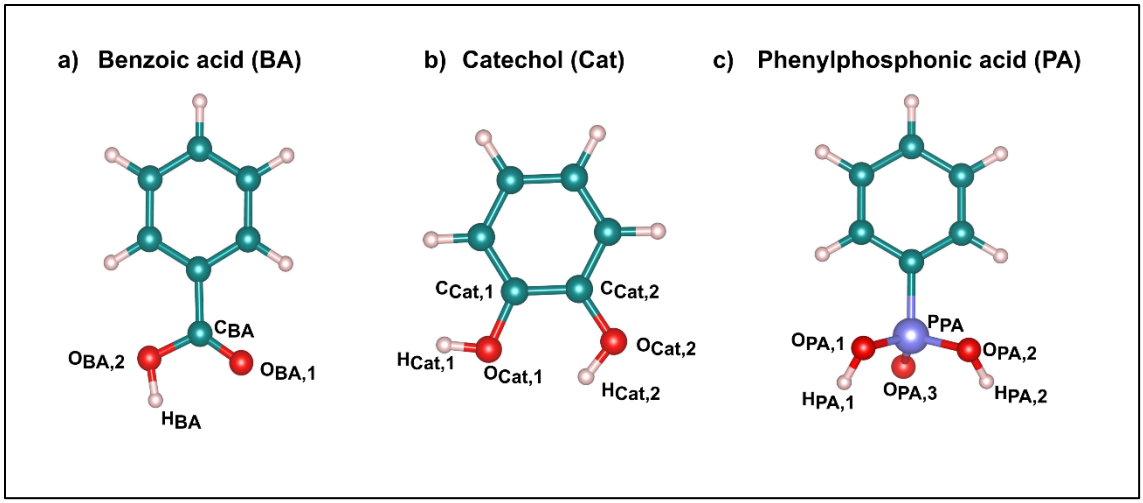

Figure 1. Molecular structure of a) Benzoic acid (BA) b) Catechol (Cat) and c) Phenylphosphonic acid (PA). The green, dark red, light blue and white spheres represent the C, O, P and H atoms of X molecule (X=BA, Cat or PA), respectively.

The work is organized as follows: the computational procedure and structural models are presented in Section 2; the results obtained for the adsorption modes BA, Cat and PA onto both clean and defective (001) WO_3 surfaces in gas phase and implicit water are given in Section 3 and finally some conclusive remarks are reported in Section 4.

2. Computational Details

2.1 Calculations Settings

All the calculations were performed using the Vienna ab initio simulation package (VASP)[91] with the projector augmented wave (PAW) approach.[92,93] The semilocal Perdew-Burke-Ernzerhof (PBE) exchange-correlation functional[94], along with the D3_BJ correction method of Grimme and co-workers[95] was employed. In order to benchmark PBE results we also performed calculations with rev-vdW-DF2 DFT functional[96] for selected configurations (see Table S1 in Supporting Information). In our calculations, the 5d and 6s (for W) and 2s and 2p electrons (for O) are treated as valence electrons. The Kohn-Sham equations were solved self-consistently with a threshold on

the energy change of 10^{-7} eV. A Gaussian smearing of 0.05 eV was used to help the total energy convergence. All the calculations were performed at Γ-point because of the large size of the employed cell (*vide infra*) with a plane-wave basis set energy cutoff of 500 eV. The structural relaxations, at both level of theory employed (PBE-D3_BJ and rev-vdW-DF2), have been carried out until all the forces were smaller than 0.02 eV/Å.

2.2 Structural Model

Primitive 32-atom unit cell of the room temperature (RT) monoclinic phase of WO_3 (space group $P2_1/n$) has been used to model the semiconductor substrate.[97] The unit cell was fully relaxed at PBE level with the D3_BJ Grimme's correction[95] to obtain lattice parameters a=7.44 Å, b=7.58 Å, c=7.76 Å, and β=90.72°, in agreement with the experimental values of a=7.31 Å, b=7.54 Å, c=7.69 Å, and β=90.9°.[98]

The stable WO_3 (001) surface with the (√2 × √2)-R45° reconstruction[99] was obtained by cleaving the crystal perpendicularly to the *c* crystallographic axis (Figure 2a). This reconstructed surface presents half a monolayer of the top oxygen atoms missing alternately along *a* and *b* directions, to avoid surface dipoles,[99] leading to 6 and 5-coordinated W atoms. Previous theoretical studies have shown that four layers for WO_3 represent a good compromise between the size of the slab (i.e. the cost of the calculation) and the accuracy of the results.[100–102] Hence, a W_xO_{3x} slab with x= 64 W atoms, corresponding to 4 layers (thickness of about 16 Å), has been adopted without freezing any layer in the structures optimizations. A vacuum space of 15 Å was used in order to avoid interactions between the replicated slabs along the *c* direction. For the calculations of isolated molecules, a cubic 30 Å-length box was used.

WO_3 is a reducible oxide and its surface can present high concentrations of oxygen vacancies, V_O, which can significantly improve the photoelectric behaviors.[49] More importantly here, V_O gives rise to local coordinative unsaturated metal atoms, possibly affecting the adsorption energy and mode on the metal oxide surface.[103] Following the procedure reported in previous works,[104–106] to model oxygen-deficient WO_3 surfaces, we have removed 1/8 of the oxygen atoms from the topmost atomic layer along the *c* axis (Figure 2b). Here we limit ourselves to investigate oxygen defects on the first surface layer, as they may more largely impact the coordination modes and their relative stability. Spin polarized calculations were performed to study oxygen defective surfaces. The ground state present a triplet spin configuration, in agreement with previous results,[104,106] with the singlet being calculated about 0.2 eV higher in energy.

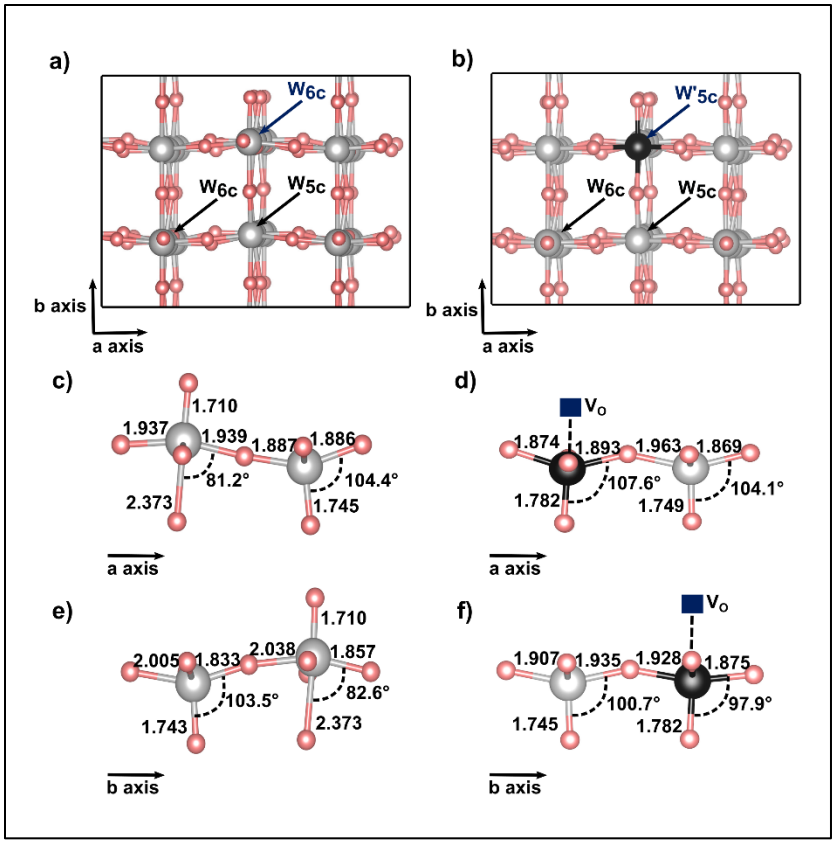

Figure 2. Representative structure of (a) clean and (b) oxygen-defective (001) WO_3 surfaces and their corresponding structural features along a ((c) and (d)) and b axes ((e) and (f)), respectively. The light grey, dark grey and light red spheres represent the W, reduced W_{6c} and O atoms of (001) WO_3 surface, respectively. Distances are in Å, angles in degrees.

2.3 Adsorption modes and adsorption energy calculations

We have considered monodentate (**M**) and bridging bidentate (**BB**) binding modes on undercoordinated tungsten surface atoms ($\mathbf{W_{5c}}$), in both molecular and dissociative (**D**) forms; in the latter. The oxydrilic H atoms were transferred to one, or more, surface O-atoms ($\mathbf{O_t}$), following the results of Ref.[104] To indicate coordination to the reduced $\mathbf{W_{6c}}$ atoms on the defective surfaces we use **M'** and **BB'** labels, for the monodentate and bidentate bridging, respectively. It is important to note that, the crystal structure of monoclinic WO_3 is characterized by a structural anisotropy

along the three cell axes, leading to an alternating long-short $W - O$ bond length[104]. Therefore, we have considered the molecule grafted to the surface along both *a* and *b* directions.

The adsorption energy, corrected by a dispersive contribution ($\Delta E_{ads} = \Delta E_{DFT} + \Delta E_{disp}$), is calculated as:

$$\Delta E_{ads} = E_{WO_3-X} - E_{WO_3} - E_X \quad (1)$$

Where, E_{WO_3-X} is the total energy of the slab with adsorbed molecule and E_{WO_3} and E_X is the total energy of the isolated slab and molecule, respectively. Thus, by definition, a negative value of ΔE_{ads} corresponds to an exothermic adsorption.

As a matter of fact, solvation effects are essential for accurate modeling of dye/semiconductor interface in realistic environment. While continuum solvation models cannot accurately describe specific interactions between the adsorbate and the surrounding solvent molecules, they are computationally fast and reasonably accurate for computing free energies in solution.[107] Here we use implicit solvation calculations to refine our estimation of the adsorption energies, by making use of the Poisson-Boltzmann model to include the dielectric screening effect of the medium as implemented in VASPsol code.[108,109] Using the relaxed geometries from gas-phase calculations, we have computed the adsorption energies in aqueous medium by performing single-point energy calculations on the gas-phase-optimized structures, with relative dielectric constant $\varepsilon = 80$ [108,110] and a Debye length of 3 Å.

3. Results and discussion

3.1 Benzoic acid

A preliminary screening of several adsorption configurations for BA on clean and defective (001) WO_3 surfaces has been performed, and here only the stable anchoring modes are reported and discussed. Table 1 lists the computed adsorption energies in vacuo and implicit water for the structures displayed in Figure 3. Some relevant optimized structural parameters for the isolated BA and the considered WO_3-anchored structures are reported in Table S2 in Supporting Information, while the changes in surface parameters upon BA adsorption on clean and defective (001) WO_3 surfaces are listed in Tables S3 and S4, respectively.

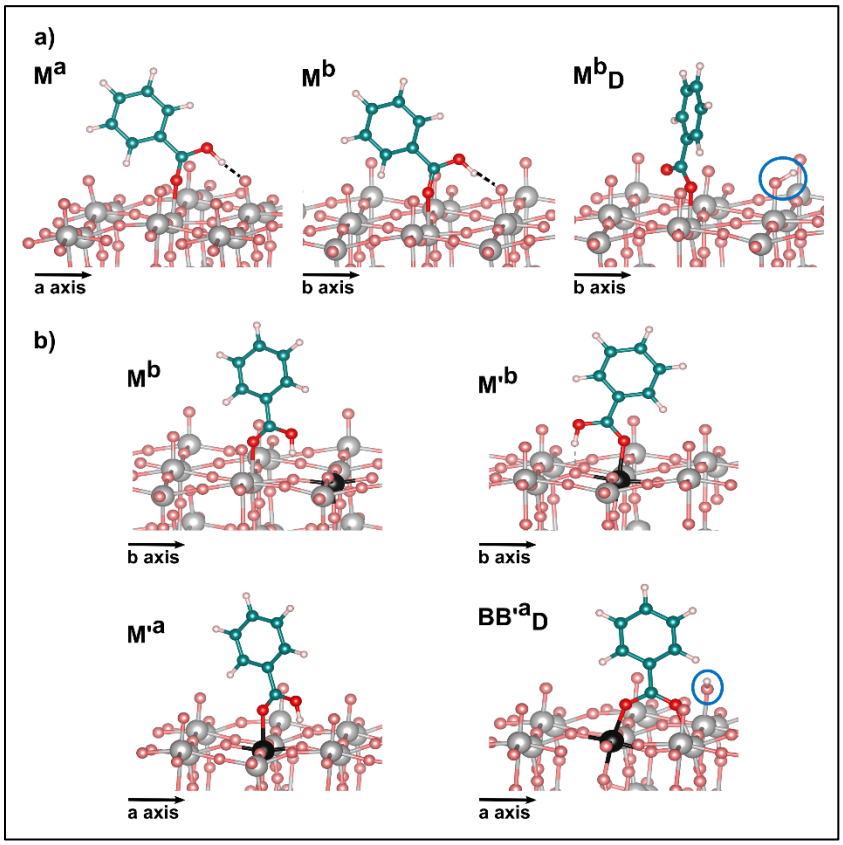

Figure 3. Optimized structure of benzoic acid on a) clean and b) defective (001) WO_3 surface. The light grey, black, and light red spheres represent the W, reduced W_{6c} and O atoms of WO_3 surface, respectively. The dark red, green and white spheres represent the O_{BA}, C and H atoms of BA molecule, respectively. Dashed lines indicate H bonding between the OH group and surface O atom.

On the clean surface, as shown in Figure 3a, no stable BB configurations were found: this is the consequence of an unfavorable $W_{5c} - W_{5c}$ distance, amounting to ~ 5.5 Å and being too large to coordinate the carboxylate group. Notice that on the TiO_2 (101) anatase surface, where the BB mode is generally the most stable one,[79] the distance between two undercoordinated Ti atoms is about 3.6 Å. Two molecular monodentate configurations, along *a* ($\mathbf{M^a}$) and *b* ($\mathbf{M^b}$) directions respectively, were found to be stable, with the latter being ca. 0.4/0.5 eV lower in energy in gas phase/solution than the former. Indeed, the new bonds formation between the molecule and surface W atoms leads to a structural rearrangement of the metal oxide surface close to the adsorption site. To take into consideration this effect, the adsorption energy can be decomposed into two opposite contributions ($\Delta E_{ads} = \Delta E_{int} + \Delta E_{def}(WO_3) + \Delta E_{def}(X)$): interaction (exothermic contribution) and deformation energies (endothermic contribution).[111,112] The computed surface deformation energies $\Delta E_{def}(WO_3)$ of the all considered configurations and their corresponding structural parameters upon BA adsorption on clean surface are reported in Tables S3 in Supporting Information. The larger structural deformation energy calculated for $\mathbf{M^a}$(0.46 eV) with respect to $\mathbf{M^b}$(0.05 eV) explains the lower stability of the former both in vacuo/implicit solvent (-1.31/-0.74 eV vs. -1.72/-1.22 eV). Finally, a dissociative M adsorption, $\mathbf{M^b_D}$ in Figure 3a, has been identified, being, however, poorly stable ($\Delta E_{ads} = -0.22$ eV in solution). Adsorption of H^+ on O_t surface atom induces an additional deformation on the surface ($\Delta E_{def}(WO_3) = 1.47$ eV), where the underneath $O_t - W_{6c,1} - O_{2p} - W_{6c,2}$ bond lengths along *c* axis change from 1.710, 2.373 and 1.759 Å to 1.881, 2.125 and 1.801 Å, respectively (see Table S3 in Supporting Information). The adsorption energies calculated for the $\mathbf{M^b}$ and $\mathbf{M^b_D}$ configurations with the rev-vdW-DF2 functional (see Table S1 in Supporting Information) are consistent and in quantitative agreement with the ones obtained with PBE+D3_BJ approach, where the dissociative $\mathbf{M^b_D}$ configuration is

less stable. Consequently, BA preferably adsorbs, on clean (001) WO_3 surface, in a molecular $\mathbf{M^b}$ binding mode forming H-bond with the O_t surface atom, with the $O_{BA,1} - W_{5c}$ and $H_{BA} - O_t$ bond lengths of 2.224 and 1.587 Å, respectively.

In the case of sub-stoichiometric WO_3 surface new configurations were considered (Figure 3b), since the molecule can coordinate either to W_{5c} or to reduced W_{6c} surface atoms. For the $\mathbf{M^b}$ configuration, due to the impossibility of forming H-bond with neighbors O_t atoms, the calculated adsorption energy is lower than the one obtained on the pristine surface (-0.78 vs -1.22 eV). On the other hand, when BA adsorbs on the reduced W_{6c} atom, in both *b* and *a* direction, ($\mathbf{M'^b}$ and $\mathbf{M'^a}$), the interaction becomes stronger, with a rather short $W - O$ distance, 2.150 and 2.127 Å, respectively (Table S2 in Supporting Information). Turning to the dissociated form, the benzoate adsorbs in a stable BB binding configuration, with the two $W - O$ bond lengths of 2.019 and 2.241 Å, for reduced W_{6c} and W_{5c}, respectively, with a strong structural rearrangement of the surface ($\Delta E_{def}(WO_3) = 2.43$ eV, Table S4). In fact, after the formation of the covalent $O_{BA} - W_{5c}$ bonds, the underneath $W_{5c} - O_{2p}$ and $W'_{5c} - O_{2p}$ bond lengths, along *c* axis, increase from 1.745 and 1.782 Å to 1.759 and 1.945 Å, respectively, while in the second layer, the $O_{2p} - W_{6c,2}$ bond lengths decrease from 2.268 and 2.002 Å to 2.244 and 1.856 Å, respectively. Significant rearrangements also involve the bond angles, with the $O_{1p} - W_{5c} - O_{2p}$ and $O_{1p} - W'_{5c} - O_{2p}$ angles decreasing by about 4° and 21°, respectively, becoming close to 81.2° of $O_{1p} - W_{6c} - O_{2p}$ angle. For this bidentate structure, the calculated adsorption energy in water is -1.16/1.23 eV at PBE+D3_BJ/ rev-vdW-DF2 level of theory, representing by far the most stable anchoring mode among the ones considered here.

Table 1. Calculated adsorption energies upon anchoring benzoic acid on the clean and defective (001) WO_3 in vacuum and implicit solvent.

Anchoring modes	In vacuum		In implicit solvent
	ΔE_{disp} (eV)	ΔE_{ads} (eV)	ΔE_{ads} (eV)
	Clean surface		
$\mathbf{M^a}$	-0.46	-1.31	-0.74
$\mathbf{M^b}$	**-0.62**	**-1.72**	**-1.22**
$\mathbf{M^b_D}$	-0.57	-0.42	-0.22
	Defective surface		
$\mathbf{M^b}$	-0.52	-1.28	-0.78
$\mathbf{M'^b}$	-0.43	-1.43	-0.95
$\mathbf{M'^a}$	-0.44	-1.43	-0.93
$\mathbf{BB'^a_D}$	**-0.56**	**-1.65**	**-1.16**

3.2 Catechol

The catechol molecule (Cat), in its molecular, mono- and bi-deprotonated forms, can be adsorbed both "perpendicularly" and "parallel" to the (001) WO_3 surface, in line with what has been observed on silica supports.[113] The calculated adsorption energies, in vacuum and water, for all the considered anchored structures shown in Figure 4, are gathered in Table 2. Table S5 in Supporting Information collects the main structural parameters obtained for the isolated Cat and anchored configurations on clean and defective (001) WO_3 surface, while Tables S6 and S7 report the

surface deformation energies and the changes in surface structural parameters upon Cat adsorption on clean and defective (001) WO_3 surfaces, respectively.

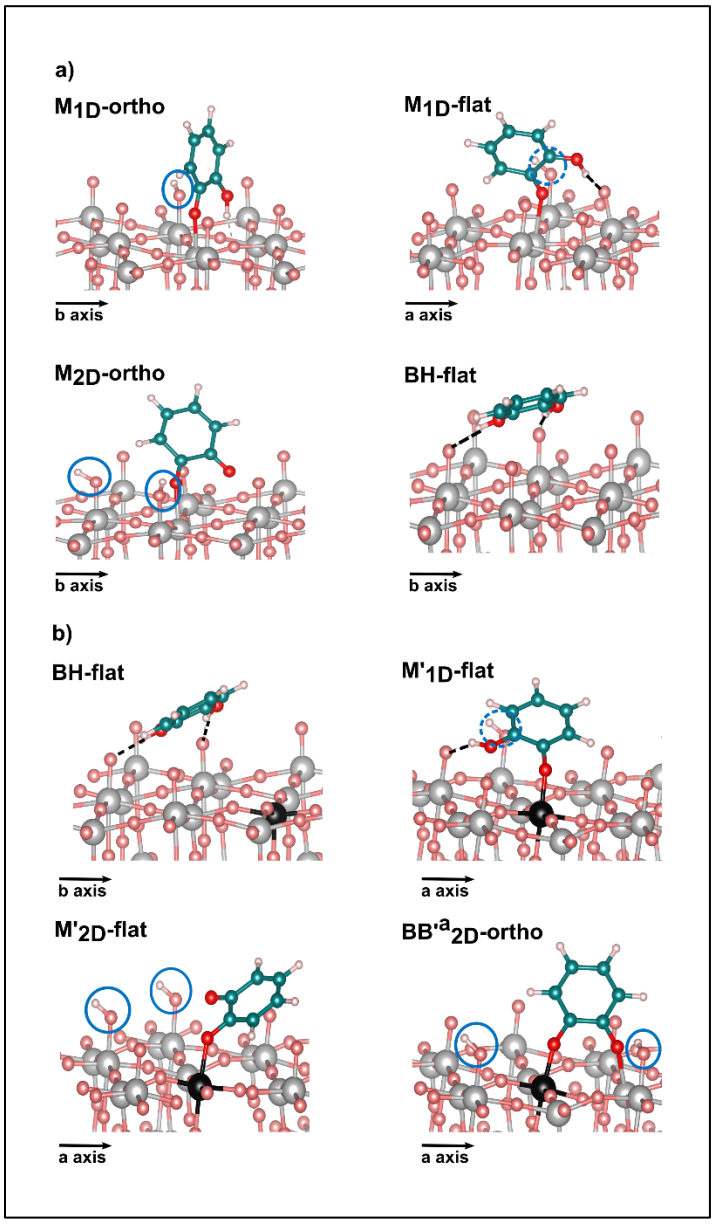

Figure 4. Optimized structure of catechol on a) clean and b) defective (001) WO_3 surface. The light grey, black, and light red spheres represent the W, reduced W_{6c} and O atoms of WO_3 surface, respectively. The dark red, green and white spheres represent the O_{Cat}, C and H atoms of Cat molecule, respectively. Dashed lines indicate H bonding between the OH group and surface O atom.

In the case of stoichiometric WO_3 surface (Figure 4a), four stable adsorption modes were identified after full structural relaxation. When Cat is in its molecular form, it can interact with the metal oxide surface in a bidentate-like mode, $\mathbf{BH-flat}$ in Figure 4a, by establishing two rather short H-bonds (ca. $1.6-1.7$ Å) with the O_t atoms on the surfaces, inducing a slight surface structural change ($\Delta E_{def}(WO_3) = -0.01$ eV). When one of the two hydroxyl groups is dissociated, by proton transfer to the surface, the preferred monodentate binding is again a "flat" configuration ($\mathbf{M_{1D}-flat}$ in Figure 4a) allowing for the formation of an H-bond with the surface, which stabilizes the covalent $O-W$ bond. These two configurations are the most stable structures calculated in solution with an adsorption energy of about 0.9 eV, whereas, in vacuo, the bidentate structure $\mathbf{BH-flat}$ is significantly more stable than the monodentate one $\mathbf{M_{1D}-flat}$ (1.60 vs. 1.38 eV). Similarly, the calculated adsorption energies of both configurations at rev-vdW-DF2 level of theory are close, with the $\mathbf{M_{1D}-flat}$ one slightly favored in solution by about 0.32 eV (0.07 eV in vacuo). The electrostatic screening of the implicit medium, indeed, more largely affects the two H-bonds with respect to the covalent O-W one, thus destabilizing the $\mathbf{BH-flat}$ structure with respect to the monodentate one. Then for the monodeprotonated Cat another, less stable (by about 0.2 eV) monodentate structure can be identified, $\mathbf{M_{1D}-ortho}$, where the molecule lies « orthogonal » to the surface plane. Finally, deprotonation of both hydroxyl groups results in a poorly stable monodentate mode, for which the calculated adsorption energy is ca. 0.50 eV; again, an unfavorable distance between the two adjacent undercoordinated W_{5c} atoms does not allow for a **BB** grafting.

As discussed above for BA, on the defective WO_3 surface, the presence of O vacancies leads to new possible configurations (see Figure 4b). For the undissociated Cat, the $\mathbf{BH-flat}$ adsorption mode, with two H-Bonds and not involving coordination to reduced W_{6c} atom, is about 0.1 eV less

stable with respect to when adsorbed on the clean surface. Then, deprotonation of one of the hydroxyl groups results in a monodentate structure, $\mathbf{M'_{1D} - flat}$, where the molecule strongly binds by his $O_{Cat,1}$ on the reduced W_{6c} atom ($O - W$ distance of 1.883 Å) forming H-bond on the surface through the undissociated OH group. By far this is the most stable structure among the ones examined here, with a computed adsorption energy of -1.11 eV; rev-vdW-DF2 results in Table S1 in Supporting Information confirm this picture, with a calculated adsorption energy in water of -1.22 eV. Also, in this case, when the molecule is fully dissociated, only a poorly stable monodentate configuration without possibility of H-bond was found, $\mathbf{M'_{2D} - flat}$, with a calculated adsorption energy of -0.47 eV. As discussed above for BA, the presence of O vacancies makes it possible to anchor the molecule in a bidentate fashion, by coordination to W_{5c} and reduced W_{6c} atoms. The resulting optimized structure is indicated as $\mathbf{BB^{/a}_{2D} - ortho}$ in Figure 4b and the computed adsorption energy is -0.88 eV, being about 0.2 eV smaller than the one calculated for the $\mathbf{M'_{1D} - flat}$ adsorption, which is thus the preferred coordination mode of Cat on sub-stochiometric WO_3 surface.

Table 2. Calculated adsorption energies upon anchoring catechol on the clean and defective (001) WO_3 in vacuum and implicit solvent.

Anchoring modes	In vacuum		In implicit solvent
	ΔE_{disp} (eV)	ΔE_{ads} (eV)	ΔE_{ads} (eV)
	Clean surface		
$M_{1D} - ortho$	-0.56	-1.16	-0.77
$M_{1D} - flat$	**-0.55**	**-1.38**	**-0.96**
$M_{2D} - ortho$	-0.50	-0.78	-0.51
$BH - flat$	**-0.57**	**-1.60**	**-0.97**
	Defective surface		
$BH - flat$	-0.49	-1.28	-0.86
$M'_{1D} - flat$	**-0.81**	**-1.60**	**-1.11**
$M'_{2D} - flat$	-0.74	-0.80	-0.47
$BB'^{a}_{2D} - ortho$	-0.66	-1.25	-0.88

3.3 Phenylphosphonic acid

Phosphonic anchoring groups are well-known to possess high affinity toward metal oxide surfaces,[114,115] offering stable anchoring in water and highly oxidative environments. According to the degree of de-protonation, $-PO_3H_2$ can react with the metal surface to form one, two, or three tungsten-oxygen covalent bonds and one or two H-bonds. The calculated adsorption energies of all the configurations considered and displayed in Figure 5 are gathered in Table 3, while Table S8 in Supporting Information compiles some relevant structural parameters for isolated and WO_3-

grafted PA. The calculated surface deformation energies and the surface deformation parameters upon anchoring PA on clean and defective surfaces are reported in Tables S9 and S10, respectively.

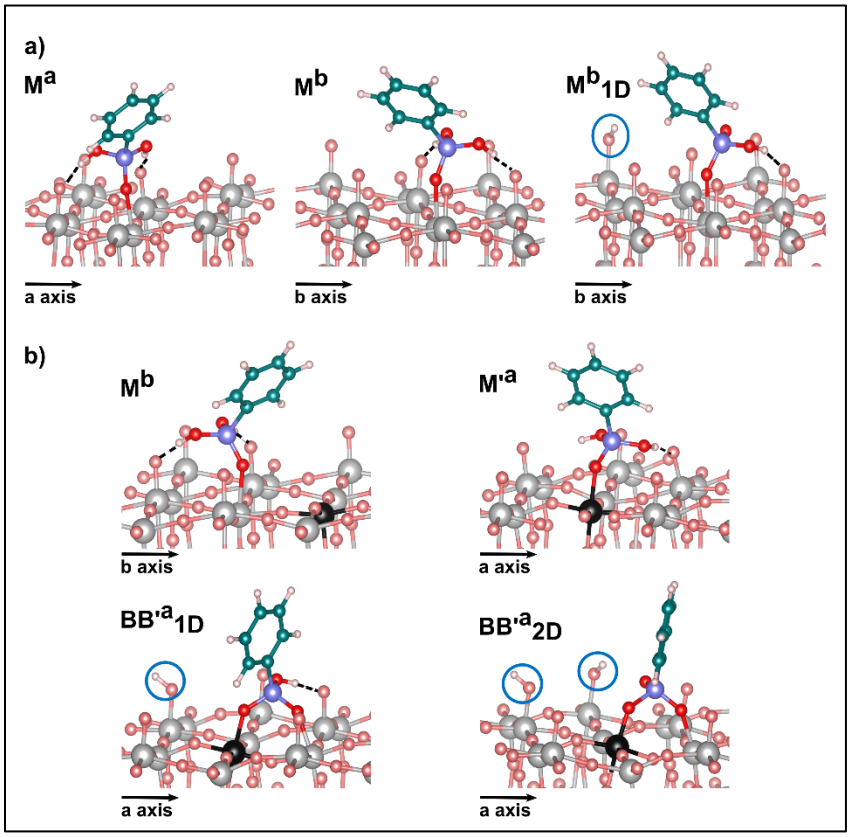

Figure 5. Optimized structure of phenylphosphonic acid on a) clean and b) defective (001) WO_3 surface. The light grey, black, and light red spheres represent the W, reduced W_{6c} and O atoms of WO_3 surface, respectively. The dark red, green, light blue and white spheres represent the O_{PA}, C, P and H atoms of PA molecule, respectively. Dashed lines indicate H bonding between the OH group and surface O atom.

The particular $W_{5c} - W_{5c}$ distances on the stoichiometric (001) WO_3 surface do not allow bidentate or tridentate binding as found on (101) TiO_2 anatase[116] and (100) NiO surfaces.[117] The possible M configurations are reported in Figure 5a, for the molecular and mono-deprotonated forms. In the undissociated case, for the monodentate anchoring with two H-bonds with O_t surface atoms the calculated adsorption energy in solution along *a* ($\mathbf{M^a}$) and *b* ($\mathbf{M^b}$) are very similar, with

the latter favored by about 0.2 eV (-1.26 and -1.42 eV respectively). This is essentially due to the contribution of the surface deformation energy, that for $\mathbf{M^a}$ turns out to be higher by about 0.15 eV than for $\mathbf{M^b}$, thus reducing the interaction energy (Tables S9 in Supporting Information). In both cases, the underneath $W_{5c} - O_{2p}$ bond length stretched to 1.77 Å with the consequent shortening of the $O_{2p} - W_{6c,2}$ bond length to 2.24 Å. Thus, the $O_{1p} - W_{5c} - O_{2p}$ angle decreases by about 6.3 and 4.7°, for $\mathbf{M^a}$ and $\mathbf{M^b}$, respectively. Then, a weakly stable (-0.19 eV) monodentate mono-deprotonated form was also found, $\mathbf{M^b_{1D}}$, in which one H-bond stabilizes the covalent $O - W$ linking.

In the sub-stoichiometric WO_3 surface, for the molecular M binding mode, we have considered the PA attached to either W_{5c} or to reduced W_{6c} surface atoms (Figure 5b). First, when the molecule adsorbs on W_{5c}, along *b* direction, $\mathbf{M^b}$, the calculated adsorption energy is -1.21 eV , slightly lower than the value obtained when PA binds to reduced W_{6c} atom along *a*, $\mathbf{M'^a}$, amounting to -1.32 eV. Then, the most stable anchoring mode is a bidentate bridging configuration for the mono-deprotonated form, $\mathbf{BB'^a_{1D}}$, where the molecule is covalently bound to a W_{5c} and to a reduced W_{6c} site, while the hydroxyl forms H-Bond with a O_t surface atom. This anchoring mode is by far the most stable one ($\Delta E_{ads} = -1.60$eV), in line with what was found for anatase TiO_2.[116] As is apparent in Table S1 in Supporting Information, a similar picture is obtained by using the rev-vdW-DF2 functional, with a predicted slightly higher adsorption energy (-1.97 eV in water). We note that similar stabilization of bidentate coordination on defective surfaces was also recently reported for delafossite $CuCrO_2$.[77] The corresponding structural features is illustrated in Figure S4-b. Finally, when the molecule is fully deprotonated, contrary to the TiO_2 and NiO case, no tridentate coordination is possible due to unfavorable disposition of coordinative

W atoms on the surface, and only a much less stable bidentate anchoring was found ($\mathbf{BB'^{a}_{2D}}$), with an adsorption energy of -0.79 eV.

Table 3. Calculated adsorption energies upon anchoring phenylphosphonic acid on the clean and defective (001) WO_3 in vacuum and implicit solvent.

Anchoring modes	In vacuum		In implicit solvent
	ΔE_{disp} (eV)	ΔE_{ads} (eV)	ΔE_{ads} (eV)
	Clean surface		
$\mathbf{M^{a}}$	-0.56	-2.12	-1.26
$\mathbf{M^{b}}$	**-0.62**	**-2.27**	**-1.42**
$\mathbf{M^{b}_{1D}}$	-0.59	-0.51	-0.19
	Defective surface		
$\mathbf{M'^{a}}$	-0.67	-2.10	-1.32
$\mathbf{M^{b}}$	-0.63	-2.02	-1.21
$\mathbf{BB'^{a}_{1D}}$	**-0.68**	**-2.40**	**-1.60**
$\mathbf{BB'^{a}_{2D}}$	-0.77	-1.24	-0.79

3.4 Summary and Conclusive Remarks

Understand the grafting behavior of anchoring groups on metal oxides such as TiO_2 and WO_3 is of high interest to design new efficient dye-sensitized photoelectrochemical cells. Until now the covalent anchoring of carboxylic acids to (101) TiO_2 anatase surfaces has been intensively investigated and most of the ab initio calculations identified the bidentate bridging mode with proton transfer to the surface as the preferred one. Calculated binding energies of monodentate modes were usually reported to be lower, although, a remarkable dependency of the relative

stability of these two adsorption modes on the level of theory can be highlighted. Concerning the phosphonic acid, while the experimental assignment of the adsorption mechanism is not available, theoretical calculations pointed to either monodentate or bidentate bridging modes as the most stable ones. Typical calculated binding energies in vacuo for bidentate coordination of carboxylic and phosphonic acids onto the most stable (101) TiO_2 anatase surface are of about 1.2 and 1.8 eV, respectively.[76] On the other hand, molecular and dissociative adsorption, in both monodentate and bidentate bridging mode, of catechol onto (101) TiO_2 anatase was reported to be less stable, with calculated adsorption energies of about 0.8-0.9 eV; although defective surfaces were shown to highly stabilize a bidentate chelating mode at about 2.5 eV.[118]

Here we have undertaken a detailed investigation on the binding mode of three anchoring groups, on clean and oxygen-defective (001) WO_3 surfaces using first principles calculations and including solvation effects and dispersion corrections. Based on the present results, both BA and PA anchoring groups are preferably adsorbed in molecular monodentate mode on clean surfaces, while the mono-deprotonated bidentate bridging binding mode becomes the preferred configuration on defective surface, in line with the findings reported by some of us for p-type (012) $CuCrO_2$ surfaces.[77] In the case of Cat molecule, favoring in all cases a flat orientation with respect to the surface plane, two configurations ($\mathrm{BH-flat}$ and $\mathrm{M_{1D}-flat}$) were found to be very close in energy in solution on clean surfaces, while it coordinates in mono-deprotonated monodentate mode on defective surfaces. A summary of the most stable adsorption energies, in implicit solvent, of the considered anchoring groups, on both clean and defective surface is displayed in Figure 6. As is apparent, these values are comparable to those discussed above for adsorption on TiO_2 anatase for the three anchoring groups, even if due to an unfavorable distance between adjacent W sites on the (001) facet, bidentate coordination can only be realized on oxygen-deficient surfaces. It is

worthwhile to stress that the possibility to realize a bidentate anchoring between the dye and the metal oxide surface has been shown to be important for maximizing the efficiency of the interfacial electron transfer processes[119] as well as for the overall device stability and performance. The present results, providing for the first time atomic-scale details on the dye anchoring mechanism on monoclinic WO_3 substrates, nicely rationalize the experimental evidence of a lower binding strength and surface coverage of carboxylic and phosphonic acids groups onto WO_3 substrates with respect to TiO_2 surfaces.[68] Our findings thus suggest novel design rules for the optimization and the selection of alternative anchoring functionalities, better matching the surface W-W patterns, for optimized WO_3-based DSSCs and hybrid photocatalysts.

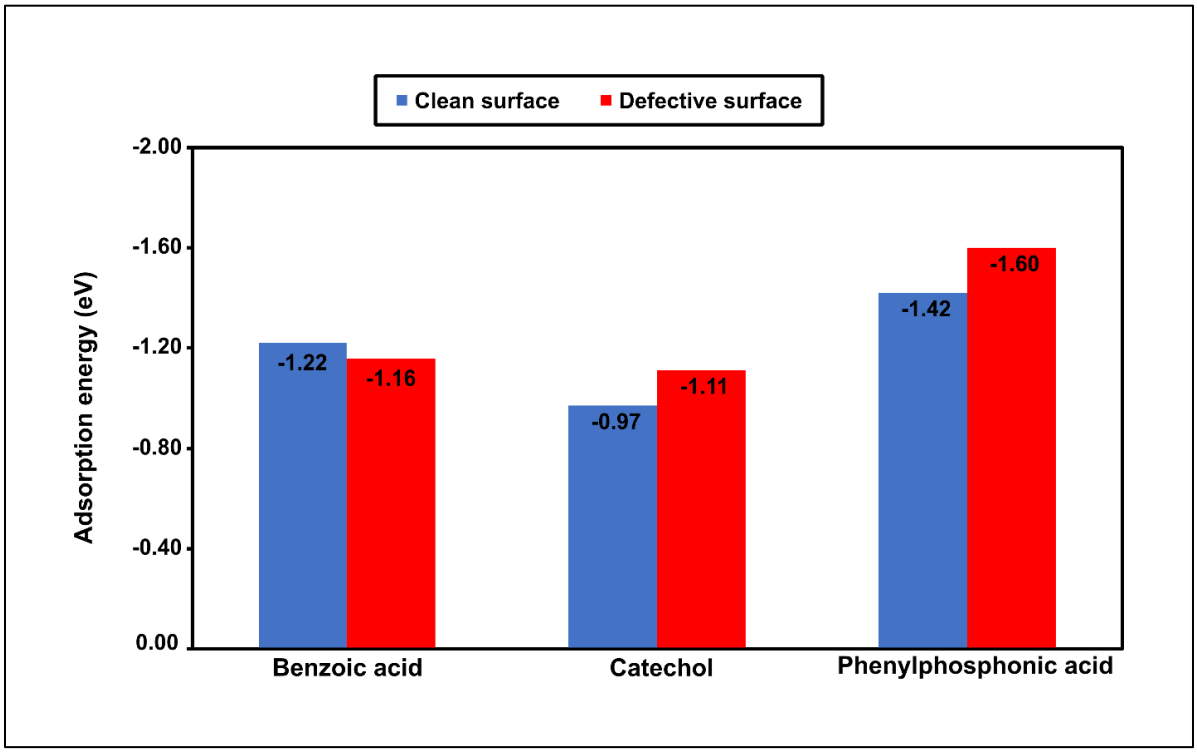

Figure 6. Calculated adsorption energies of benzoic acid, catechol and phenylphosphonic acid on clean and defective surfaces in implicit solvent.

Supporting Information. Calculated adsorption energies using PBE+D3_BJ and rev-vdW-DF2 functionals in vacuo and solution for Benzoic acid, catechol and phenylphosphonic acid on both clean and defective surfaces; Surfaces deformation energies calculations and parameters changes in the 2 first layers of clean and defective surfaces upon molecules adsorption; Optimized structural parameters of isolated clean and defective (001) WO_3 surfaces, isolated molecules, and anchored configurations on both clean and defective surfaces (PDF). Coordinates of the optimized configurations on clean and defective (001) WO_3 surfaces in POSCAR format (ZIP).

Acknowledgement. M.P. and M. B. are grateful to the financial support given by the COMETE project (COnception in silico de Matériaux pour l'EnvironnemenT et l'Energie), which is co-funded by the European Union under the program 'FEDER-FSE Lorraine et Massif des Vosges 2014-2020.

References

(1) Concepcion, J. J.; House, R. L.; Papanikolas, J. M.; Meyer, T. J. Chemical Approaches to Artificial Photosynthesis. *Proc. Natl. Acad. Sci.* **2012**, *109* (39), 15560–15564. https://doi.org/10.1073/pnas.1212254109.

(2) Young, K. J.; Martini, L. A.; Milot, R. L.; Snoeberger, R. C.; Batista, V. S.; Schmuttenmaer, C. A.; Crabtree, R. H.; Brudvig, G. W. Light-Driven Water Oxidation for Solar Fuels. *Coord. Chem. Rev.* **2012**, *256* (21–22), 2503–2520. https://doi.org/10.1016/j.ccr.2012.03.031.

(3) Hamann, T. W. An Adaptive Junction. *Nat. Mater.* **2014**, *13* (1), 3–4. https://doi.org/10.1038/nmat3843.

(4) Armaroli, N.; Balzani, V. Solar Electricity and Solar Fuels: Status and Perspectives in the Context of the Energy Transition. *Chem. - Eur. J.* **2016**, *22* (1), 32–57. https://doi.org/10.1002/chem.201503580.

(5) Detz, R. J.; Reek, J. N. H.; Zwaan, B. C. C. van der. The Future of Solar Fuels: When Could They Become Competitive? *Energy Environ. Sci.* **2018**, *11* (7), 1653–1669. https://doi.org/10.1039/C8EE00111A.

(6) Anscombe, N. Solar Cells That Mimic Plants. *Nat. Photonics* **2011**, *5* (5), 266–267. https://doi.org/10.1038/nphoton.2011.67.

(7) Yu, Z.; Li, F.; Sun, L. Recent Advances in Dye-Sensitized Photoelectrochemical Cells for Solar Hydrogen Production Based on Molecular Components. *Energy Environ. Sci.* **2015**, *8* (3), 760–775. https://doi.org/10.1039/C4EE03565H.

(8) Collomb, M.-N.; Morales, D. V.; Astudillo, C. N.; Dautreppe, B.; Fortage, J. Hybrid Photoanodes for Water Oxidation Combining a Molecular Photosensitizer with a Metal

Oxide Oxygen-Evolving Catalyst. *Sustain. Energy Fuels* **2019**, *4* (1), 31–49. https://doi.org/10.1039/C9SE00597H.

(9) Yun, S.; Vlachopoulos, N.; Qurashi, A.; Ahmad, S.; Hagfeldt, A. Dye Sensitized Photoelectrolysis Cells. *Chem. Soc. Rev.* **2019**, *48* (14), 3705–3722. https://doi.org/10.1039/C8CS00987B.

(10) Brennaman, M. K.; Dillon, R. J.; Alibabaei, L.; Gish, M. K.; Dares, C. J.; Ashford, D. L.; House, R. L.; Meyer, G. J.; Papanikolas, J. M.; Meyer, T. J. Finding the Way to Solar Fuels with Dye-Sensitized Photoelectrosynthesis Cells. *J. Am. Chem. Soc.* **2016**, *138* (40), 13085–13102. https://doi.org/10.1021/jacs.6b06466.

(11) Li, F.; Fan, K.; Xu, B.; Gabrielsson, E.; Daniel, Q.; Li, L.; Sun, L. Organic Dye-Sensitized Tandem Photoelectrochemical Cell for Light Driven Total Water Splitting. *J. Am. Chem. Soc.* **2015**, *137* (28), 9153–9159. https://doi.org/10.1021/jacs.5b04856.

(12) Han, K.; Wang, M.; Zhang, S.; Wu, S.; Yang, Y.; Sun, L. Photochemical Hydrogen Production from Water Catalyzed by CdTe Quantum Dots/Molecular Cobalt Catalyst Hybrid Systems. *Chem. Commun.* **2015**, *51* (32), 7008–7011. https://doi.org/10.1039/C5CC00536A.

(13) Wang, M.; Han, K.; Zhang, S.; Sun, L. Integration of Organometallic Complexes with Semiconductors and Other Nanomaterials for Photocatalytic H2 Production. *Coord. Chem. Rev.* **2015**, *287*, 1–14. https://doi.org/10.1016/j.ccr.2014.12.005.

(14) Chandrasekaran, S.; Kaeffer, N.; Cagnon, L.; Aldakov, D.; Fize, J.; Nonglaton, G.; Baleras, F.; Mailley, P.; Artero, V. A Robust ALD-Protected Silicon-Based Hybrid Photoelectrode for Hydrogen Evolution under Aqueous Conditions. *Chem. Sci.* **2019**, *10* (16), 4469–4475. https://doi.org/10.1039/C8SC05006F.

(15) Liang, Y.; Huang, X.; Huang, Y.; Wang, X.; Li, F.; Wang, Y.; Tian, F.; Liu, B.; Shen, Z. X.; Cui, T. New Metallic Ordered Phase of Perovskite $CsPbI_3$ under Pressure. *Adv. Sci.* **2019**, *6* (14), 1900399. https://doi.org/10.1002/advs.201900399.

(16) Walter, M. G.; Warren, E. L.; McKone, J. R.; Boettcher, S. W.; Mi, Q.; Santori, E. A.; Lewis, N. S. Solar Water Splitting Cells. *Chem. Rev.* **2010**, *110* (11), 6446–6473. https://doi.org/10.1021/cr1002326.

(17) Chen, X.; Shen, S.; Guo, L.; Mao, S. S. Semiconductor-Based Photocatalytic Hydrogen Generation. *Chem. Rev.* **2010**, *110* (11), 6503–6570. https://doi.org/10.1021/cr1001645.

(18) Leung, J. J.; Warnan, J.; Nam, D. H.; Zhang, J. Z.; Willkomm, J.; Reisner, E. Photoelectrocatalytic H_2 Evolution in Water with Molecular Catalysts Immobilised on p-Si via a Stabilising Mesoporous TiO_2 Interlayer. *Chem. Sci.* **2017**, *8* (7), 5172–5180. https://doi.org/10.1039/C7SC01277B.

(19) Wadsworth, B. L.; Beiler, A. M.; Khusnutdinova, D.; Jacob, S. I.; Moore, G. F. Electrocatalytic and Optical Properties of Cobaloxime Catalysts Immobilized at a Surface-Grafted Polymer Interface. *ACS Catal.* **2016**, *6* (12), 8048–8057. https://doi.org/10.1021/acscatal.6b02194.

(20) Chandrasekaran, S.; Macdonald, T. J.; Mange, Y. J.; Voelcker, N. H.; Nann, T. A Quantum Dot Sensitized Catalytic Porous Silicon Photocathode. *J Mater Chem A* **2014**, *2* (25), 9478–9481. https://doi.org/10.1039/C4TA01677G.

(21) Liu, B.; Li, X.-B.; Gao, Y.-J.; Li, Z.-J.; Meng, Q.-Y.; Tung, C.-H.; Wu, L.-Z. A Solution-Processed, Mercaptoacetic Acid-Engineered CdSe Quantum Dot Photocathode for Efficient Hydrogen Production under Visible Light Irradiation. *Energy Environ. Sci.* **2015**, *8* (5), 1443–1449. https://doi.org/10.1039/C5EE00331H.

(22) Gu, J.; Yan, Y.; Young, J. L.; Steirer, K. X.; Neale, N. R.; Turner, J. A. Water Reduction by a P-GaInP2 Photoelectrode Stabilized by an Amorphous TiO2 Coating and a Molecular Cobalt Catalyst. *Nat. Mater.* **2016**, *15* (4), 456–460. https://doi.org/10.1038/nmat4511.

(23) Li, W.; Sheehan, S. W.; He, D.; He, Y.; Yao, X.; Grimm, R. L.; Brudvig, G. W.; Wang, D. Hematite-Based Solar Water Splitting in Acidic Solutions: Functionalization by Mono- and Multilayers of Iridium Oxygen-Evolution Catalysts. *Angew. Chem. Int. Ed.* **2015**, *54* (39), 11428–11432. https://doi.org/10.1002/anie.201504427.

(24) Chen, X.; Fu, Y.; Kong, T.; Shang, Y.; Niu, F.; Diao, Z.; Shen, S. Protected Hematite Nanorod Arrays with Molecular Complex Co-Catalyst for Efficient and Stable Photoelectrochemical Water Oxidation: Protected Hematite Nanorod Arrays with Molecular Complex Co-Catalyst for Efficient and Stable Photoelectrochemical Water Oxidation. *Eur. J. Inorg. Chem.* **2019**, *2019* (15), 2078–2085. https://doi.org/10.1002/ejic.201801200.

(25) Zhong, D. K.; Zhao, S.; Polyansky, D. E.; Fujita, E. Diminished Photoisomerization of Active Ruthenium Water Oxidation Catalyst by Anchoring to Metal Oxide Electrodes. *J. Catal.* **2013**, *307*, 140–147. https://doi.org/10.1016/j.jcat.2013.07.018.

(26) Tong, H.; Jiang, Y.; Zhang, Q.; Li, J.; Jiang, W.; Zhang, D.; Li, N.; Xia, L. Enhanced Interfacial Charge Transfer on a Tungsten Trioxide Photoanode with Immobilized Molecular Iridium Catalyst. *ChemSusChem* **2017**, *10* (16), 3268–3275. https://doi.org/10.1002/cssc.201700721.

(27) Liu, B.; Li, J.; Wu, H.-L.; Liu, W.-Q.; Jiang, X.; Li, Z.-J.; Chen, B.; Tung, C.-H.; Wu, L.-Z. Improved Photoelectrocatalytic Performance for Water Oxidation by Earth-Abundant Cobalt Molecular Porphyrin Complex-Integrated $BiVO_4$ Photoanode. *ACS Appl. Mater. Interfaces* **2016**, *8* (28), 18577–18583. https://doi.org/10.1021/acsami.6b04510.

(28) Wan, X.; Wang, L.; Dong, C.-L.; Menendez Rodriguez, G.; Huang, Y.-C.; Macchioni, A.; Shen, S. Activating Kläui-Type Organometallic Precursors at Metal Oxide Surfaces for Enhanced Solar Water Oxidation. *ACS Energy Lett.* **2018**, *3* (7), 1613–1619. https://doi.org/10.1021/acsenergylett.8b00847.

(29) Ye, S.; Ding, C.; Chen, R.; Fan, F.; Fu, P.; Yin, H.; Wang, X.; Wang, Z.; Du, P.; Li, C. Mimicking the Key Functions of Photosystem II in Artificial Photosynthesis for Photoelectrocatalytic Water Splitting. *J. Am. Chem. Soc.* **2018**, *140* (9), 3250–3256. https://doi.org/10.1021/jacs.7b10662.

(30) Matheu, R.; Moreno-Hernandez, I. A.; Sala, X.; Gray, H. B.; Brunschwig, B. S.; Llobet, A.; Lewis, N. S. Photoelectrochemical Behavior of a Molecular Ru-Based Water-Oxidation Catalyst Bound to TiO_2 -Protected Si Photoanodes. *J. Am. Chem. Soc.* **2017**, *139* (33), 11345–11348. https://doi.org/10.1021/jacs.7b06800.

(31) Giraudeau, A.; Fan, F.-R. F.; Bard, A. J. Semiconductor Electrodes. 30. Spectral Sensitization of the Semiconductors Titanium Oxide (n-TiO2) and Tungsten Oxide (n-WO3) with Metal Phthalocyanines. *J. Am. Chem. Soc.* **1980**, *102* (16), 5137–5142. https://doi.org/10.1021/ja00536a001.

(32) Zhao, Z.; Butburee, T.; Peerakiatkhajohn, P.; Lyu, M.; Wang, S.; Wang, L.; Zheng, H. Carbon Quantum Dots Sensitized Vertical WO_3 Nanoplates with Enhanced Photoelectrochemical Properties. *ChemistrySelect* **2016**, *1* (11), 2772–2777. https://doi.org/10.1002/slct.201600718.

(33) Zheng, H.; Tachibana, Y.; Kalantar-zadeh, K. Dye-Sensitized Solar Cells Based on WO_3. *Langmuir* **2010**, *26* (24), 19148–19152. https://doi.org/10.1021/la103692y.
(34) Hara, K.; Zhao, Z.-G.; Cui, Y.; Miyauchi, M.; Miyashita, M.; Mori, S. Nanocrystalline Electrodes Based on Nanoporous-Walled WO_3 Nanotubes for Organic-Dye-Sensitized Solar Cells. *Langmuir* **2011**, *27* (20), 12730–12736. https://doi.org/10.1021/la201639f.
(35) Ronconi, F.; Syrgiannis, Z.; Bonasera, A.; Prato, M.; Argazzi, R.; Caramori, S.; Cristino, V.; Bignozzi, C. A. Modification of Nanocrystalline WO_3 with a Dicationic Perylene Bisimide: Applications to Molecular Level Solar Water Splitting. *J. Am. Chem. Soc.* **2015**, *137* (14), 4630–4633. https://doi.org/10.1021/jacs.5b01519.
(36) Kirner, J. T.; Finke, R. G. Sensitization of Nanocrystalline Metal Oxides with a Phosphonate-Functionalized Perylene Diimide for Photoelectrochemical Water Oxidation with a CoO_x Catalyst. *ACS Appl. Mater. Interfaces* **2017**, *9* (33), 27625–27637. https://doi.org/10.1021/acsami.7b05874.
(37) Sheehan, S. W.; Thomsen, J. M.; Hintermair, U.; Crabtree, R. H.; Brudvig, G. W.; Schmuttenmaer, C. A. A Molecular Catalyst for Water Oxidation That Binds to Metal Oxide Surfaces. *Nat. Commun.* **2015**, *6* (1), 6469. https://doi.org/10.1038/ncomms7469.
(38) Klepser, B. M.; Bartlett, B. M. Anchoring a Molecular Iron Catalyst to Solar-Responsive WO_3 Improves the Rate and Selectivity of Photoelectrochemical Water Oxidation. *J. Am. Chem. Soc.* **2014**, *136* (5), 1694–1697. https://doi.org/10.1021/ja4086808.
(39) Sarnowska, M.; Bienkowski, K.; Barczuk, P. J.; Solarska, R.; Augustynski, J. Highly Efficient and Stable Solar Water Splitting at (Na)WO_3 Photoanodes in Acidic Electrolyte Assisted by Non-Noble Metal Oxygen Evolution Catalyst. *Adv. Energy Mater.* **2016**, *6* (14), 1600526. https://doi.org/10.1002/aenm.201600526.
(40) Hu, X.; Zheng, X.-J.; Li, Y.; Ma, D.-K. Bipyridine-Co 2+ Molecular Catalyst Modified WO 3 Nanoplate Arrays Photoanode with Enhanced Photoelectrochemical Activity. *Mater. Lett.* **2018**, *220*, 36–39. https://doi.org/10.1016/j.matlet.2018.02.109.
(41) Wei, P.; Lin, K.; Meng, D.; Xie, T.; Na, Y. Photoelectrochemical Performance for Water Oxidation Improved by Molecular Nickel Porphyrin-Integrated WO_3 /TiO_2 Photoanode. *ChemSusChem* **2018**, *11* (11), 1746–1750. https://doi.org/10.1002/cssc.201800705.
(42) Zhao, Y.; Yan, X.; Yang, K. R.; Cao, S.; Dong, Q.; Thorne, J. E.; Materna, K. L.; Zhu, S.; Pan, X.; Flytzani-Stephanopoulos, M.; Brudvig, G. W.; Batista, V. S.; Wang, D. End-On Bound Iridium Dinuclear Heterogeneous Catalysts on WO_3 for Solar Water Oxidation. *ACS Cent. Sci.* **2018**, *4* (9), 1166–1172. https://doi.org/10.1021/acscentsci.8b00335.
(43) Huber, F. L.; Amthor, S.; Schwarz, B.; Mizaikoff, B.; Streb, C.; Rau, S. Multi-Phase Real-Time Monitoring of Oxygen Evolution Enables *in Operando* Water Oxidation Catalysis Studies. *Sustain. Energy Fuels* **2018**, *2* (9), 1974–1978. https://doi.org/10.1039/C8SE00328A.
(44) Ding, J.; Chai, Y.; Liu, Q.; Liu, X.; Ren, J.; Dai, W.-L. Selective Deposition of Silver Nanoparticles onto WO3 Nanorods with Different Facets: The Correlation of Facet-Induced Electron Transport Preference and Photocatalytic Activity. *J. Phys. Chem. C* **2016**, *120* (8), 4345–4353. https://doi.org/10.1021/acs.jpcc.5b10580.
(45) Diez-Cabanes, V.; Morales-García, Á.; Illas, F.; Pastore, M. Understanding the Structural and Electronic Properties of Photoactive Tungsten Oxide Nanoparticles from Density Functional Theory and GW Approaches. *J. Chem. Theory Comput.* **2021**, *17* (6), 3462–3470. https://doi.org/10.1021/acs.jctc.1c00293.

(46) Mi, Q.; Zhanaidarova, A.; Brunschwig, B. S.; Gray, H. B.; Lewis, N. S. A Quantitative Assessment of the Competition between Water and Anion Oxidation at WO3 Photoanodes in Acidic Aqueous Electrolytes. *Energy Environ. Sci.* **2012**, *5* (2), 5694–5700. https://doi.org/10.1039/C2EE02929D.

(47) Yourey, J. E.; Bartlett, B. M. Electrochemical Deposition and Photoelectrochemistry of CuWO4, a Promising Photoanode for Water Oxidation. *J. Mater. Chem.* **2011**, *21* (21), 7651–7660. https://doi.org/10.1039/C1JM11259G.

(48) Lin, R.; Wan, J.; Xiong, Y.; Wu, K.; Cheong, W.; Zhou, G.; Wang, D.; Peng, Q.; Chen, C.; Li, Y. Quantitative Study of Charge Carrier Dynamics in Well-Defined WO3 Nanowires and Nanosheets: Insight into the Crystal Facet Effect in Photocatalysis. *J. Am. Chem. Soc.* **2018**, *140* (29), 9078–9082. https://doi.org/10.1021/jacs.8b05293.

(49) Berak, J. M.; Sienko, M. J. Effect of Oxygen-Deficiency on Electrical Transport Properties of Tungsten Trioxide Crystals. *J. Solid State Chem.* **1970**, *2* (1), 109–133. https://doi.org/10.1016/0022-4596(70)90040-X.

(50) Zhang, T.; Zhu, Z.; Chen, H.; Bai, Y.; Xiao, S.; Zheng, X.; Xue, Q.; Yang, S. Iron-Doping-Enhanced Photoelectrochemical Water Splitting Performance of Nanostructured WO3: A Combined Experimental and Theoretical Study. *Nanoscale* **2015**, *7* (7), 2933–2940. https://doi.org/10.1039/C4NR07024K.

(51) Anik, M.; Osseo-Asare, K. Effect of PH on the Anodic Behavior of Tungsten. *J. Electrochem. Soc.* **2002**, *149* (6), B224–B233. https://doi.org/10.1149/1.1471544.

(52) Corby, S.; Francàs, L.; Selim, S.; Sachs, M.; Blackman, C.; Kafizas, A.; Durrant, J. R. Water Oxidation and Electron Extraction Kinetics in Nanostructured Tungsten Trioxide Photoanodes. *J. Am. Chem. Soc.* **2018**, *140* (47), 16168–16177. https://doi.org/10.1021/jacs.8b08852.

(53) Calbo, J.; Pastore, M.; Mosconi, E.; Ortí, E.; De Angelis, F. Computational Modeling of Single- versus Double-Anchoring Modes in Di-Branched Organic Sensitizers on TiO_2 Surfaces: Structural and Electronic Properties. *Phys Chem Chem Phys* **2014**, *16* (10), 4709–4719. https://doi.org/10.1039/C3CP54970D.

(54) Gupta, K. S. V.; Zhang, J.; Marotta, G.; Reddy, M. A.; Singh, S. P.; Islam, A.; Han, L.; De Angelis, F.; Chandrasekharam, M.; Pastore, M. Effect of the Anchoring Group in the Performance of Carbazole-Phenothiazine Dyads for Dye-Sensitized Solar Cells. *Dyes Pigments* **2015**, *113*, 536–545. https://doi.org/10.1016/j.dyepig.2014.09.032.

(55) Yu, J.; Wang, W.; Cheng, B.; Su, B.-L. Enhancement of Photocatalytic Activity of Mesporous TiO_2 Powders by Hydrothermal Surface Fluorination Treatment. *J. Phys. Chem. C* **2009**, *113* (16), 6743–6750. https://doi.org/10.1021/jp900136q.

(56) Ambrosio, F.; Martsinovich, N.; Troisi, A. What Is the Best Anchoring Group for a Dye in a Dye-Sensitized Solar Cell? *J. Phys. Chem. Lett.* **2012**, *3* (11), 1531–1535. https://doi.org/10.1021/jz300520p.

(57) Zhang, L.; Cole, J. M. Anchoring Groups for Dye-Sensitized Solar Cells. *ACS Appl. Mater. Interfaces* **2015**, *7* (6), 3427–3455. https://doi.org/10.1021/am507334m.

(58) Galoppini, E. Linkers for Anchoring Sensitizers to Semiconductor Nanoparticles. *Coord. Chem. Rev.* **2004**, *248* (13–14), 1283–1297. https://doi.org/10.1016/j.ccr.2004.03.016.

(59) Moreira, N. H.; Domınguez, A.; Frauenheim, T.; da Rosa, A. L. On the Stabilization Mechanisms of Organic Functional Groups on ZnO Surfaces. *Phys. Chem. Chem. Phys.* **2012**, *14* (44), 15445. https://doi.org/10.1039/c2cp42435e.

(60) Martsinovich, N.; Troisi, A. Theoretical Studies of Dye-Sensitised Solar Cells: From Electronic Structure to Elementary Processes. *Energy Environ. Sci.* **2011**, *4* (11), 4473. https://doi.org/10.1039/c1ee01906f.
(61) Ignatchenko, A. V. Density Functional Theory Study of Carboxylic Acids Adsorption and Enolization on Monoclinic Zirconia Surfaces. *J. Phys. Chem. C* **2011**, *115* (32), 16012–16018. https://doi.org/10.1021/jp203381h.
(62) Muñoz-García, A. B.; Caputo, L.; Schiavo, E.; Baiano, C.; Maddalena, P.; Pavone, M. Ab Initio Study of Anchoring Groups for CuGaO2 Delafossite-Based p-Type Dye Sensitized Solar Cells. *Front. Chem.* **2019**, *7*, 158. https://doi.org/10.3389/fchem.2019.00158.
(63) Hagfeldt, A.; Boschloo, G.; Sun, L.; Kloo, L.; Pettersson, H. Dye-Sensitized Solar Cells. *Chem. Rev.* **2010**, *110* (11), 6595–6663. https://doi.org/10.1021/cr900356p.
(64) Péchy, P.; Rotzinger, F. P.; Nazeeruddin, M. K.; Kohle, O.; Zakeeruddin, S. M.; Humphry-Baker, R.; Grätzel, M. Preparation of Phosphonated Polypyridyl Ligands to Anchor Transition-Metal Complexes on Oxide Surfaces: Application for the Conversion of Light to Electricity with Nanocrystalline TiO2 Films. *J. Chem. Soc. Chem. Commun.* **1995**, No. 1, 65–66. https://doi.org/10.1039/C39950000065.
(65) Zhang, B.; Wang, H.; Xi, J.; Zhao, F.; Zeng, B. In Situ Formation of Inorganic/Organic Heterojunction Photocatalyst of WO3/Au/Polydopamine for Immunoassay of Human Epididymal Protein 4. *Electrochimica Acta* **2020**, *331*, 135350. https://doi.org/10.1016/j.electacta.2019.135350.
(66) Park, S.-M.; Nam, C. Dye-Adsorption Properties of WO3 Nanorods Grown by Citric Acid Assisted Hydrothermal Methods. *Ceram. Int.* **2017**, *43* (18), 17022–17025. https://doi.org/10.1016/j.ceramint.2017.09.111.
(67) Adhikari, S.; Mandal, S.; Sarkar, D.; Kim, D.-H.; Madras, G. Kinetics and Mechanism of Dye Adsorption on WO3 Nanoparticles. *Appl. Surf. Sci.* **2017**, *420*, 472–482. https://doi.org/10.1016/j.apsusc.2017.05.191.
(68) Esarey, S. L.; Bartlett, B. M. PH-Dependence of Binding Constants and Desorption Rates of Phosphonate- and Hydroxamate-Anchored $[Ru(Bpy)_3]^{2+}$ on TiO_2 and WO_3. *Langmuir* **2018**, *34* (15), 4535–4547. https://doi.org/10.1021/acs.langmuir.8b00263.
(69) Bishop, L. M.; Yeager, J. C.; Chen, X.; Wheeler, J. N.; Torelli, M. D.; Benson, M. C.; Burke, S. D.; Pedersen, J. A.; Hamers, R. J. A Citric Acid-Derived Ligand for Modular Functionalization of Metal Oxide Surfaces via "Click" Chemistry. *Langmuir* **2012**, *28* (2), 1322–1329. https://doi.org/10.1021/la204145t.
(70) Wang, Y.; Zeng, J.; Zhou, Z.; Shen, G.; Tang, T.; Sagar, R. U. R.; Qi, X. Growth of a High-Performance WO3 Nanofilm Directly on a Polydopamine-Modified ITO Electrode for Electrochromism and Power Storage Applications. *Appl. Surf. Sci.* **2022**, *573*, 151603. https://doi.org/10.1016/j.apsusc.2021.151603.
(71) Ma, S.; Amar, F. G.; Frederick, B. G. Surface Heterogeneity and Diffusion in the Desorption of Methanol from WO3(001) Surfaces. *J. Phys. Chem. A* **2003**, *107* (9), 1413–1423. https://doi.org/10.1021/jp0222292.
(72) Ma, S.; Frederick, B. G. Reactions of Aliphatic Alcohols on WO3(001) Surfaces. *J. Phys. Chem. B* **2003**, *107* (43), 11960–11969. https://doi.org/10.1021/jp035383c.
(73) Zhao, Y.; Balasubramanyam, S.; Sinha, R.; Lavrijsen, R.; Verheijen, M. A.; Bol, A. A.; Bieberle-Hütter, A. Physical and Chemical Defects in WO_3 Thin Films and Their Impact

on Photoelectrochemical Water Splitting. *ACS Appl. Energy Mater.* **2018**, *1* (11), 5887–5895. https://doi.org/10.1021/acsaem.8b00849.

(74) Elbohy, H.; Reza, K. M.; Abdulkarim, S.; Qiao, Q. Creation of Oxygen Vacancies to Activate WO3 for Higher Efficiency Dye-Sensitized Solar Cells. *Sustain. Energy Fuels* **2018**, *2* (2), 403–412. https://doi.org/10.1039/C7SE00483D.

(75) Vittadini, A.; Selloni, A.; Rotzinger, F. P.; Grätzel, M. Formic Acid Adsorption on Dry and Hydrated TiO2 Anatase (101) Surfaces by DFT Calculations. *J. Phys. Chem. B* **2000**, *104* (6), 1300–1306. https://doi.org/10.1021/jp993583b.

(76) Nilsing, M.; Lunell, S.; Persson, P.; Ojamäe, L. Phosphonic Acid Adsorption at the TiO2 Anatase (101) Surface Investigated by Periodic Hybrid HF-DFT Computations. *Surf. Sci.* **2005**, *582* (1–3), 49–60. https://doi.org/10.1016/j.susc.2005.02.044.

(77) Dimple, D.; Lebègue, S.; Pastore, M. Dye Anchoring on $CuCrO_2$ Surfaces for p-Type Dye-Sensitized Solar Cell Applications: An Ab Initio Study. *ACS Appl. Energy Mater.* **2021**, *4* (6), 6180–6190. https://doi.org/10.1021/acsaem.1c00970.

(78) Pastore, M.; De Angelis, F. Modeling Materials and Processes in Dye-Sensitized Solar Cells: Understanding the Mechanism, Improving the Efficiency; Springer Berlin Heidelberg: Berlin, Heidelberg, 2013. https://doi.org/10.1007/128_2013_468.

(79) Anselmi, C.; Mosconi, E.; Pastore, M.; Ronca, E.; De Angelis, F. Adsorption of Organic Dyes on TiO2 Surfaces in Dye-Sensitized Solar Cells: Interplay of Theory and Experiment. *Phys. Chem. Chem. Phys.* **2012**, *14* (46), 15963. https://doi.org/10.1039/c2cp43006a.

(80) Evanko, C. R.; Dzombak, D. A. Influence of Structural Features on Sorption of NOM-Analogue Organic Acids to Goethite. *Environ. Sci. Technol.* **1998**, *32* (19), 2846–2855. https://doi.org/10.1021/es980256t.

(81) Jenkins, A. H.; Medlin, J. W. Controlling Heterogeneous Catalysis with Organic Monolayers on Metal Oxides. *Acc. Chem. Res.* **2021**, *54* (21), 4080–4090. https://doi.org/10.1021/acs.accounts.1c00469.

(82) Ellis, L. D.; Trottier, R. M.; Musgrave, C. B.; Schwartz, D. K.; Medlin, J. W. Controlling the Surface Reactivity of Titania via Electronic Tuning of Self-Assembled Monolayers. *ACS Catal.* **2017**, *7* (12), 8351–8357. https://doi.org/10.1021/acscatal.7b02789.

(83) Paredes-Gil, K.; Páez-Hernández, D.; Arratia-Pérez, R.; Mendizábal, F. Insights into the Role of D-A-π-A Type pro-Aromatic Organic Dyes with Thieno[3,4-b]Pyrazine as A Acceptor Group into Dye-Sensitized Solar-Cells. A TD-DFT/Periodic DFT Study. *Int. J. Quantum Chem.* **2020**, *120* (5), e26108. https://doi.org/10.1002/qua.26108.

(84) Roy, J. K.; Kar, S.; Leszczynski, J. Insight into the Optoelectronic Properties of Designed Solar Cells Efficient Tetrahydroquinoline Dye-Sensitizers on TiO2(101) Surface: First Principles Approach. *Sci. Rep.* **2018**, *8* (1), 10997. https://doi.org/10.1038/s41598-018-29368-9.

(85) Geldof, D.; Tassi, M.; Carleer, R.; Adriaensens, P.; Roevens, A.; Meynen, V.; Blockhuys, F. Binding Modes of Phosphonic Acid Derivatives Adsorbed on TiO2 Surfaces: Assignments of Experimental IR and NMR Spectra Based on DFT/PBC Calculations. *Surf. Sci.* **2017**, *655*, 31–38. https://doi.org/10.1016/j.susc.2016.09.001.

(86) Ford, W. E.; Abraham, F.; Scholz, F.; Nelles, G.; Sandford, G.; Wrochem, F. von. Spectroscopic Characterization of Fluorinated Benzylphosphonic Acid Monolayers on AlOx/Al Surfaces. *J. Phys. Chem. C* **2017**, *121* (3), 1690–1703. https://doi.org/10.1021/acs.jpcc.6b11089.

(87) Nilsing, M.; Persson, P.; Lunell, S.; Ojamäe, L. Dye-Sensitization of the TiO_2 Rutile (110) Surface by Perylene Dyes: Quantum-Chemical Periodic B3LYP Computations. *J. Phys. Chem. C* **2007**, *111* (32), 12116–12123. https://doi.org/10.1021/jp072253l.
(88) O'Rourke, C.; Bowler, D. R. DSSC Anchoring Groups: A Surface Dependent Decision. *J. Phys. Condens. Matter* **2014**, *26* (19), 195302. https://doi.org/10.1088/0953-8984/26/19/195302.
(89) Li, J.; Nilsing, M.; Kondov, I.; Wang, H.; Persson, P.; Lunell, S.; Thoss, M. Dynamical Simulation of Photoinduced Electron Transfer Reactions in Dye−Semiconductor Systems with Different Anchor Groups. *J. Phys. Chem. C* **2008**, *112* (32), 12326–12333. https://doi.org/10.1021/jp7118263.
(90) Sánchez, V. M.; de la Llave, E.; Scherlis, D. A. Adsorption of R−OH Molecules on TiO_2 Surfaces at the Solid−Liquid Interface. *Langmuir* **2011**, *27* (6), 2411–2419. https://doi.org/10.1021/la103511c.
(91) Kresse, G.; Hafner, J. *Ab Initio* Molecular Dynamics for Liquid Metals. *Phys. Rev. B* **1993**, *47* (1), 558–561. https://doi.org/10.1103/PhysRevB.47.558.
(92) Blöchl, P. E. Projector Augmented-Wave Method. *Phys. Rev. B* **1994**, *50* (24), 17953–17979. https://doi.org/10.1103/PhysRevB.50.17953.
(93) Kresse, G.; Joubert, D. From Ultrasoft Pseudopotentials to the Projector Augmented-Wave Method. *Phys. Rev. B* **1999**, *59* (3), 1758–1775. https://doi.org/10.1103/PhysRevB.59.1758.
(94) Perdew, J. P.; Burke, K.; Ernzerhof, M. Generalized Gradient Approximation Made Simple. *Phys. Rev. Lett.* **1996**, *77* (18), 3865–3868. https://doi.org/10.1103/PhysRevLett.77.3865.
(95) Grimme, S.; Ehrlich, S.; Goerigk, L. Effect of the Damping Function in Dispersion Corrected Density Functional Theory. *J. Comput. Chem.* **2011**, *32* (7), 1456–1465. https://doi.org/10.1002/jcc.21759.
(96) Hamada, I. Van Der Waals Density Functional Made Accurate. *Phys. Rev. B* **2014**, *89* (12), 121103. https://doi.org/10.1103/PhysRevB.89.121103.
(97) Woodward, P. M.; Sleight, A. W.; Vogt, T. Structure Refinement of Triclinic Tungsten Trioxide. *J. Phys. Chem. Solids* **1995**, *56* (10), 1305–1315. https://doi.org/10.1016/0022-3697(95)00063-1.
(98) Loopstra, B. O.; Rietveld, H. M. Further Refinement of the Structure of WO3. *Acta Crystallogr. Sect. B* **1969**, *25* (7), 1420–1421. https://doi.org/10.1107/S0567740869004146.
(99) Jin, H.; Zhu, J.; Hu, J.; Li, Y.; Zhang, Y.; Huang, X.; Ding, K.; Chen, W. Structural and Electronic Properties of Tungsten Trioxides: From Cluster to Solid Surface. *Theor. Chem. Acc.* **2011**, *130* (1), 103–114. https://doi.org/10.1007/s00214-011-0996-7.
(100) Ping, Y.; Goddard, W. A.; Galli, G. A. Energetics and Solvation Effects at the Photoanode/Catalyst Interface: Ohmic Contact versus Schottky Barrier. *J. Am. Chem. Soc.* **2015**, *137* (16), 5264–5267. https://doi.org/10.1021/jacs.5b00798.
(101) Oison, V.; Saadi, L.; Lambert-Mauriat, C.; Hayn, R. Mechanism of CO and O3 Sensing on WO3 Surfaces: First Principle Study. *Sens. Actuators B Chem.* **2011**, *160* (1), 505–510. https://doi.org/10.1016/j.snb.2011.08.018.
(102) Lambert-Mauriat, C.; Oison, V.; Saadi, L.; Aguir, K. Ab Initio Study of Oxygen Point Defects on Tungsten Trioxide Surface. *Surf. Sci.* **2012**, *606* (1–2), 40–45. https://doi.org/10.1016/j.susc.2011.08.018.

(103) Liu, L.; Lin, M.; Liu, Z.; Sun, H.; Zhao, X. Density Functional Theory Study of CO2 and H2O Adsorption on a Monoclinic WO3(001) Surface. *Chem. Res. Chin. Univ.* **2017**, *33* (2), 255–260. https://doi.org/10.1007/s40242-017-6378-5.
(104) Albanese, E.; Di Valentin, C.; Pacchioni, G. H_2O Adsorption on WO_3 and WO_{3-x} (001) Surfaces. *ACS Appl. Mater. Interfaces* **2017**, *9* (27), 23212–23221. https://doi.org/10.1021/acsami.7b06139.
(105) Zhang, L.; Wen, B.; Zhu, Y.-N.; Chai, Z.; Chen, X.; Chen, M. First-Principles Calculations of Water Adsorption on Perfect and Defect WO3(0 0 1). *Comput. Mater. Sci.* **2018**, *150*, 484–490. https://doi.org/10.1016/j.commatsci.2018.04.056.
(106) Gerosa, M.; Gygi, F.; Govoni, M.; Galli, G. The Role of Defects and Excess Surface Charges at Finite Temperature for Optimizing Oxide Photoabsorbers. *Nat. Mater.* **2018**, *17* (12), 1122–1127. https://doi.org/10.1038/s41563-018-0192-4.
(107) Tomasi, J.; Cammi, R.; Mennucci, B.; Cappelli, C.; Corni, S. Molecular Properties in Solution Described with a Continuum Solvation Model. *Phys. Chem. Chem. Phys.* **2002**, *4* (23), 5697–5712. https://doi.org/10.1039/B207281P.
(108) Mathew, K.; Hennig, R. G. Implicit Self-Consistent Description of Electrolyte in Plane-Wave Density-Functional Theory. *arXiv:1601.03346* **2016**.
(109) Mathew, K.; Sundararaman, R.; Letchworth-Weaver, K.; Arias, T. A.; Hennig, R. G. Implicit Solvation Model for Density-Functional Study of Nanocrystal Surfaces and Reaction Pathways. *J. Chem. Phys.* **2014**, *140* (8), 084106. https://doi.org/10.1063/1.4865107.
(110) Petrosyan, S. A.; Rigos, A. A.; Arias, T. A. Joint Density-Functional Theory: Ab Initio Study of Cr2O3 Surface Chemistry in Solution. *J. Phys. Chem. B* **2005**, *109* (32), 15436–15444. https://doi.org/10.1021/jp044822k.
(111) Valero, M.; Raybaud, P.; Sautet, P. Interplay between Molecular Adsorption and Metal–Support Interaction for Small Supported Metal Clusters: CO and C2H4 Adsorption on Pd4/ΓPd4/γ-Al2O3. *J. Catal.* **2007**, *247* (2), 339–355. https://doi.org/10.1016/j.jcat.2007.02.014.
(112) Hurtado-Aular, O.; Vidal, A. B.; Sierraalta, A.; Añez, R. Periodic DFT Study of Water Adsorption on M-WO3(001), m-WO3(100), h-WO3(001) and h-WO3(100). Role of Hydroxyl Groups on the Stability of Polar Hexagonal Surfaces. *Surf. Sci.* **2020**, *694*, 121558. https://doi.org/10.1016/j.susc.2019.121558.
(113) Mian, S. A.; Saha, L. C.; Jang, J.; Wang, L.; Gao, X.; Nagase, S. Density Functional Theory Study of Catechol Adhesion on Silica Surfaces. *J. Phys. Chem. C* **2010**, *114* (48), 20793–20800. https://doi.org/10.1021/jp1070538.
(114) Luschtinetz, R.; Frenzel, J.; Milek, T.; Seifert, G. Adsorption of Phosphonic Acid at the TiO_2 Anatase (101) and Rutile (110) Surfaces. *J. Phys. Chem. C* **2009**, *113* (14), 5730–5740. https://doi.org/10.1021/jp8110343.
(115) Woodward, J. T.; Ulman, A.; Schwartz, D. K. Self-Assembled Monolayer Growth of Octadecylphosphonic Acid on Mica. *Langmuir* **1996**, *12* (15), 3626–3629. https://doi.org/10.1021/la9510689.
(116) Pastore, M.; De Angelis, F. First-Principles Modeling of a Dye-Sensitized TiO_2 /IrO_2 Photoanode for Water Oxidation. *J. Am. Chem. Soc.* **2015**, *137* (17), 5798–5809. https://doi.org/10.1021/jacs.5b02128.

(117) Piccinin, S.; Rocca, D.; Pastore, M. Role of Solvent in the Energy Level Alignment of Dye-Sensitized NiO Interfaces. *J. Phys. Chem. C* **2017**, *121* (40), 22286–22294. https://doi.org/10.1021/acs.jpcc.7b08463.

(118) Xu, Y.; Chen, W.-K.; Liu, S.-H.; Cao, M.-J.; Li, J.-Q. Interaction of Photoactive Catechol with TiO2 Anatase (101) Surface: A Periodic Density Functional Theory Study. *Chem. Phys.* **2007**, *331* (2–3), 275–282. https://doi.org/10.1016/j.chemphys.2006.10.018.

(119) Pastore, M.; De Angelis, F. Computational Modelling of TiO_2 Surfaces Sensitized by Organic Dyes with Different Anchoring Groups: Adsorption Modes, Electronic Structure and Implication for Electron Injection/Recombination. *Phys Chem Chem Phys* **2012**, *14* (2), 920–928. https://doi.org/10.1039/C1CP22663K.
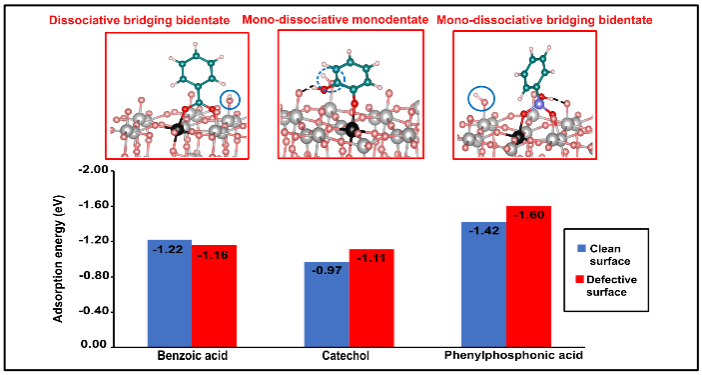
TOC Graphic